

# Textbook efficiency: massively parallel matrix-free multigrid for the Stokes system

Nils Kohl\*      Ulrich Rde\*†

## Abstract

We employ textbook multigrid efficiency (TME), as introduced by Achi Brandt, to construct an asymptotically optimal monolithic multigrid solver for the Stokes system. The geometric multigrid solver builds upon the concept of hierarchical hybrid grids (HHG), which is extended to higher-order finite-element discretizations, and a corresponding matrix-free implementation. The computational cost of the full multigrid (FMG) iteration is quantified, and the solver is applied to multiple benchmark problems. Through a parameter study, we suggest configurations that achieve TME for both, stabilized equal-order, and Taylor-Hood discretizations. The excellent node-level performance of the relevant compute kernels is presented via a roofline analysis. Finally, we demonstrate the weak and strong scalability to up to 147,456 parallel processes and solve Stokes systems with more than  $3.6 \times 10^{12}$  (trillion) unknowns.

**Key words** multigrid, textbook efficiency, hierarchical hybrid grids, parallel computing, finite element method, Stokes problem

**AMS subject classifications** 65F10, 65N30, 65N55

## 1 Introduction

Textbook multigrid efficiency (TME), a term coined by Achi Brandt in [18, 48], suggests that an ideal multigrid algorithm should solve a discrete system with less than 10 times the computational work that is required to apply the corresponding operator.

The computational work  $\mathfrak{W}(M)$  required to employ a numerical method  $M$ , in order to solve a linear system  $Ax = b$ , is conveniently expressed in multiples of a work unit (WU). One WU amounts to the computational work  $\mathfrak{W}(A)$  required for application of the considered linear operator, i. e.

$$1\text{WU} := \mathfrak{W}(A). \quad (1)$$

Consequently, we achieve TME if we design a multigrid method MG, that solves  $Ax = b$ , with

$$\frac{\mathfrak{W}(\text{MG})}{\mathfrak{W}(A)} < 10. \quad (2)$$

We emphasize that TME is defined with respect to the underlying *differential* equation. Solving the partial differential equation (PDE) with optimal complexity is a

---

\*Chair for System Simulation (LSS), Friedrich-Alexander Universitt Erlangen-Nrnberg, Germany ([nils.kohl@fau.de](mailto:nils.kohl@fau.de), [ulrich.ruede@fau.de](mailto:ulrich.ruede@fau.de))

†Centre Europen de Recherche et de Formation Avance en Calcul Scientifique (CERFACS), France

more ambitious goal and is potentially more difficult to achieve than only showing the mesh independent *algebraic* convergence of an iterative solver. To evaluate whether an algorithm reaches TME, also the specific PDE must be well defined, including the (class of) boundary conditions and forcing terms under consideration.

With a proclaimed cost of only 10 WU, the TME paradigm sets a concrete quantitative limit of the cost for solving the PDE. In this sense, reaching TME is again more challenging than the notion of asymptotic optimality as it is typically shown in abstract multigrid convergence results. In the latter case the constants remain unspecified so that no comparison of the efficiency between different methods is possible. However, though fundamentally desirable, the strong notion of TME efficiency is yet rarely discussed in the literature and, in fact, has not been demonstrated for many algorithms or problems.

For this article, we specifically point out that to reach TME for higher order discretizations must be expected to be more difficult than for low order discretizations. We identify three effects that will usually drive up the cost for solving linear systems in a TME setting for higher order discretizations.

- First, we must not forget that the cost of a WU itself will typically increase with the order of discretization, most typically because a plain higher order stiffness matrix will have more nonzero entries and is thus more densely populated.
- The linear system for higher order discretization may be less well suited for an iterative solution, typically it exhibits a higher condition number so that, e.g., Krylov methods may need more iterations to reach the same error tolerance as for equivalent low order systems
- Finally, and possibly most intriguingly, the expected cost for a nested iteration will grow. While for a typical  $\mathcal{O}(h^2)$  discretization, the error is expected to improve asymptotically by a factor of 4 per level of canonical mesh refinement  $h \rightarrow h/2$ , this factor increases to 16 for a  $\mathcal{O}(h^4)$  discretization. This means that in full multigrid (FMG) [19], each new level for a high order discretization must enforce also much stricter algebraic convergence than for low order. Where a single v-cycle on each level may be enough for low order, for high order it may well be that two or more v-cycles will become necessary.

Additionally, we note that the denser matrix structure and higher flop cost of higher order discretizations is sometimes considered to be an advantage, since it leads to more flops per memory operations in the iterative solver. This is then termed a better *algorithmic balance* [34]. A better algorithmic balance may help to better exploit computer architectures whose memory throughput is poor compared to their peak floating point operations per second (FLOPS).

The solvers considered in this article are built on top of the hierarchical hybrid grids (HHG) structure [15, 13, 30, 10, 29, 31, 7]. In previous work, the efficiency, performance, and extreme scalability of matrix-free multigrid solvers based on HHG have been demonstrated for linear, nodal discretizations. A main contribution of this paper is, besides the construction of an efficient geometric multigrid solver, the extension of HHG to higher-order discretizations.

The SIAM review article [43] provides a broad overview over the relevance of fast numerical methods for the solution of PDEs. Besides the standard literature on multigrid solvers [19, 50, 33], there is exhaustive research that cannot be referenced in its entirety. Various smoothers for the solution of elliptic problems are presented in [51, 17, 1, 42, 52]. The relevance of matrix-free methods is underlined e.g. in [5, 21, 39, 42, 44]. Domain specific languages and code generation are rather current approaches towards fast iterative solvers [40]. Apart from geometric multigrid solvers, algebraic multigrid methods are an efficient alternative, especially for problems on unstructured grids [3], as well as massively solvers based on domain decomposition [24, 37, 56].

In this article, we consider the Stokes system as model problem. Discretization with finite-elements yields a linear system with saddle-point structure. Section 2 covers the discretization and introduces the parallel data structures of the matrix-free implementation. After definition of the multigrid components in section 3, we quantify the computational cost of the resulting FMG iteration in section 4. Finally, in section 5, we present numerical benchmarks to find optimal solver configurations in the sense of TME, and demonstrate the node-level performance as well as the parallel scalability of the implementation.

## 2 Finite element discretization for the Stokes system

As model problem we consider the constant-coefficient Stokes system that describes viscous fluid motion on a bounded, polyhedral domain  $\Omega \subset \mathbb{R}^3$ , defined by

$$\begin{aligned} -\Delta \mathbf{u} + \nabla p &= \mathbf{f} \\ \nabla \cdot \mathbf{u} &= 0 \end{aligned} \quad (3)$$

where  $\mathbf{u} = (u_1, u_2, u_3)^\top$  represents the vector-valued velocity field,  $p$  the scalar pressure field, and  $\mathbf{f} = (f_1, f_2, f_3)^\top$  an external force acting on the fluid. We consider Dirichlet, and natural Neumann outflow boundary conditions on  $\partial\Omega = \partial\Omega_D \cup \partial\Omega_N$

$$\mathbf{u} = \mathbf{w} \text{ on } \partial\Omega_D, \quad \frac{\partial \mathbf{u}}{\partial \mathbf{n}} = \mathbf{np} \text{ on } \partial\Omega_N$$

where  $\mathbf{n}$  is the outward pointing normal at the boundary. If  $\partial\Omega = \partial\Omega_D$ , the pressure is defined up to a constant and the Dirichlet boundary function  $\mathbf{w}$  must satisfy compatibility conditions [26]. We fix  $p$  to a mean value of 0 by setting  $\int_\Omega p \, dx = 0$ .

Let  $\mathcal{T}_0$  denote an unstructured partitioning of the computational domain into tetrahedral elements. Each of the elements in  $\mathcal{T}_0$  is then successively and uniformly refined according to [16], yielding a hierarchy of tetrahedral meshes  $\mathcal{T} = \{\mathcal{T}_\ell, \ell = 0, \dots, L\}$ . The structured refinement of a single coarse grid tetrahedron is illustrated in fig. 1. The mesh hierarchy is discussed in more detail in sections 2.1 and 2.2.

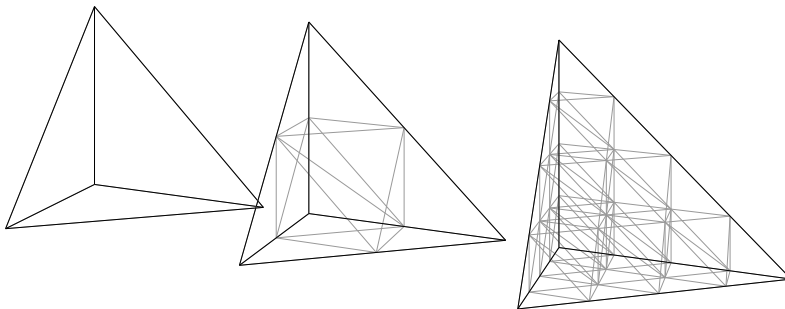


Figure 1: Uniform, structured refinement of a single tetrahedron of the unstructured mesh. From left to right: initial tetrahedron, refinement level  $\ell = 1$ , refinement level  $\ell = 2$ .

We define the solution and test spaces  $\mathbf{H}_E^1$  and  $\mathbf{H}_{E_0}^1$

$$\mathbf{H}_E^1 := \{\mathbf{u} \in \mathcal{H}^1(\Omega)^3 : \mathbf{u} = \mathbf{w} \text{ on } \partial\Omega_D\}, \quad \mathbf{H}_{E_0}^1 := \{\mathbf{v} \in \mathcal{H}^1(\Omega)^3 : \mathbf{v} = 0 \text{ on } \partial\Omega_D\},$$

and standard conforming finite element spaces  $\mathbf{V}_0^\ell \subset \mathbf{H}_{E_0}^1$ ,  $\mathbf{V}_E^\ell \subset \mathbf{H}_E^1$ , and  $Q^\ell \subset L_2(\Omega)$  defined by polynomial functions on each tetrahedron for each level  $\ell$  of the mesh hierarchy.

The standard weak formulation of eq. (3) is [26]: find  $\mathbf{u}_\ell \in \mathbf{V}_E^\ell$  and  $p_\ell \in Q^\ell$  with

$$\begin{aligned} \int_{\Omega} \nabla \mathbf{u}_\ell : \nabla \mathbf{v}_\ell - \int_{\Omega} p_\ell \nabla \cdot \mathbf{v}_\ell &= \int_{\Omega} \mathbf{f} \cdot \mathbf{v}_\ell \quad \text{for all } \mathbf{v}_\ell \in \mathbf{V}_0^\ell \\ \int_{\Omega} q_\ell \nabla \cdot \mathbf{u}_\ell &= 0 \quad \text{for all } q_\ell \in Q^\ell. \end{aligned} \quad (4)$$

With basis functions  $\{\Phi_j\}$  of  $\mathbf{V}_E^\ell$  and  $\{\psi_j\}$  of  $Q^\ell$ , we define coefficient vectors  $\underline{\mathbf{u}}_\ell \in \mathbb{R}^{n_u}$ ,  $\underline{\mathbf{p}}_\ell \in \mathbb{R}^{n_p}$ ,  $\underline{\mathbf{f}}_\ell \in \mathbb{R}^{n_u}$ , and  $\underline{\mathbf{g}}_\ell \in \mathbb{R}^{n_p}$  by

$$\mathbf{u}_\ell = \sum_{j=1}^{n_u+n_\partial} \underline{\mathbf{u}}_{\ell,j} \Phi_j, \quad p_\ell = \sum_{j=1}^{n_p} \underline{\mathbf{p}}_{\ell,j} \psi_j,$$

where  $\sum_{j=1}^{n_u} \underline{\mathbf{u}}_{\ell,j} \Phi_j \in \mathbf{V}_0^\ell$ , and  $\sum_{j=n_u+1}^{n_u+n_\partial} \underline{\mathbf{u}}_{\ell,j} \Phi_j$  interpolates the boundary function  $\mathbf{w}$  on  $\partial\Omega_D$ .

The discrete formulation of eq. (4) on level  $\ell$  results in the saddle point problem

$$\mathcal{A}_\ell \begin{bmatrix} \underline{\mathbf{u}}_\ell \\ \underline{\mathbf{p}}_\ell \end{bmatrix} = \begin{bmatrix} \underline{\mathbf{f}}_\ell \\ \underline{\mathbf{g}}_\ell \end{bmatrix}, \quad \mathcal{A}_\ell = \begin{bmatrix} \mathbf{A}_\ell & \mathbf{B}_\ell^\top \\ \mathbf{B}_\ell & -C_\ell \end{bmatrix}, \quad \mathbf{A}_\ell = \text{diag}(A_{x,\ell}, A_{y,\ell}, A_{z,\ell}) \quad (5)$$

where  $\mathbf{A}_\ell \in \mathbb{R}^{n_u \times n_u}$  is the discrete, block-diagonal vector-Laplacian,  $A_\ell := A_{x,\ell} = A_{y,\ell} = A_{z,\ell}$  the scalar Laplacian, and  $\mathbf{B}_\ell \in \mathbb{R}^{n_p \times n_u}$  represents the divergence matrix, with

$$\mathbf{a}_{ij} = \int_{\Omega} \nabla \Phi_i : \nabla \Phi_j, \quad \mathbf{b}_{kj} = - \int_{\Omega} \psi_k \nabla \cdot \Phi_j.$$

The right hand side of eq. (5) is given by

$$\underline{\mathbf{f}}_{\ell,j} = \int_{\Omega} \Phi_j \cdot \mathbf{f} - \sum_{j=n_u+1}^{n_u+n_\partial} \underline{\mathbf{u}}_{\ell,j} \int_{\Omega} \nabla \Phi_i : \nabla \Phi_j, \quad \underline{\mathbf{g}}_{\ell,k} = - \sum_{j=n_u+1}^{n_u+n_\partial} \underline{\mathbf{u}}_{\ell,j} - \int_{\Omega} \psi_k \nabla \cdot \Phi_j.$$

The approximation spaces  $\mathbf{V}_0^\ell$ ,  $\mathbf{V}_E^\ell$ , and  $Q^\ell$  must be chosen carefully, to assert uniform inf-sup stability [26]. Two common choices are stabilized equal-order, linear finite elements for velocity and pressure ( $\mathbf{P}_1 - \mathbf{P}_1$  approximation) [36], and the stable pairing of quadratic elements for the velocity and linear elements for the pressure ( $\mathbf{P}_2 - \mathbf{P}_1$  approximation), also referred to as *Taylor-Hood* method [47]. For the stable  $\mathbf{P}_2 - \mathbf{P}_1$  approximation,  $C_\ell = 0$  in eq. (5). The  $\mathbf{P}_1 - \mathbf{P}_1$  approximation requires additional stabilization. We employ the Pressure Stabilized Petrov-Galerkin (PSPG) stabilization [20, 36] by setting  $C_\ell$  according to

$$c_{ij} = \sum_{T \in \mathcal{T}_\ell} \delta_T h_T^2 \int_T \nabla \psi_i \cdot \nabla \psi_j, \quad i, j = 1, \dots, n_p \quad (6)$$

where  $h_T = (\int_T dx)^{1/3}$  depends on the size of the element  $T$ , and  $\delta_T$  is chosen as  $1/12$  [25]. The right-hand side block vector  $\underline{\mathbf{g}}_\ell$  must be modified accordingly at the Dirichlet boundary [25].

## 2.1 Hierarchical hybrid grids

Support for unstructured grids is arguably one of the major advantages of the finite element method. However, unstructured grids may complicate the implementation of geometric multigrid methods, and efficient matrix-free compute kernels that are essential for solving extreme-scale problems [10, 29]. Fully structured meshes, on

the other hand, often cannot adequately represent real-world domains. Hierarchical hybrid grids (HHG) [14, 15, 13, 30, 7] are one attempt to combine the best of both worlds.

During the refinement of the coarsest grid  $\mathcal{T}_0$ , all new tetrahedra are geometrically identical (up to translation) to one out of six different tetrahedra [14, 16]. Also, the edges at each inner node of the mesh span a geometrically identical *stencil* [13, 30]. The stencil at an unknown is defined by its coupling to other unknowns, potentially including itself. In the finite element context, this corresponds to the non-zero entries of a row in the globally assembled system matrix. The invariant topology of the stencil in the uniformly refined tetrahedron has some important implications. In particular, unknowns can be updated in a node-centered, stencil-based fashion. This may result in performance advantages and it simplifies the realization of operators that require the diagonal entries of the system matrix (e.g. Gauss-Seidel smoothers) [30]. Additionally, for operators with constant coefficients, the stencil values are constant at each node inside a refined coarse grid tetrahedron, providing even more optimization opportunities. Moreover, the successive refinement yields a grid hierarchy suitable for geometric multigrid methods by design.

The block-structured domain partitioning allows defining entirely distributed data structures that are crucial for extreme-scalable simulations [6, 32]. To communicate data between the refined tetrahedra (also called macro-cells), we introduce *interface primitives* [14, 15, 38]. For each face, edge, and vertex of the unstructured coarse mesh, a separate face-, edge-, or vertex-primitive data structure is created. In the following we will refer to them as macro-faces, macro-edges and macro-vertices, respectively. Figure 2 shows a macro-face primitive that interfaces two neighboring macro-cells. Each macro-primitive, including the interface primitives, is assigned to

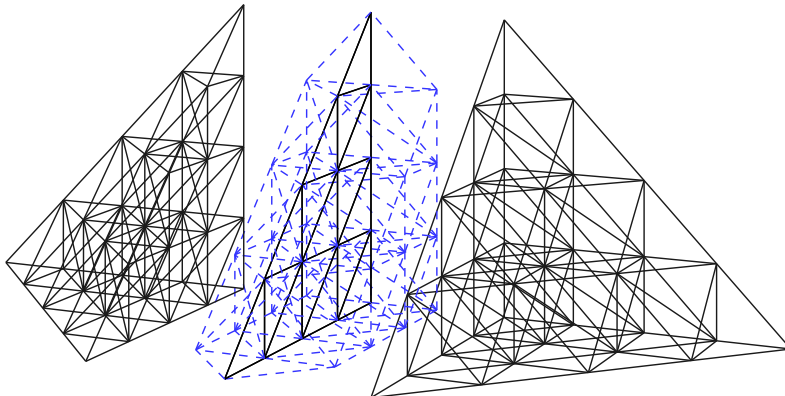


Figure 2: Macro-face primitive that interfaces two macro-cells. Each of the three primitives can be distributed to arbitrary parallel processes. The dashed lines indicate ghost-layer data.

exactly one of the parallel processes. Note that one process may thus hold multiple macro-primitives. Each grid point of the refined mesh is assigned to exactly one macro-primitive. To allow for read access to neighboring unknowns, the macro-primitives are extended by ghost-layers. When necessary, i.e., usually before operator applications, the ghost-layers are updated by communication between neighboring macro-primitives.

The primitives are connected, such that they can be interpreted as a graph, where the graph-vertices correspond to the primitives, and the graph-edges correspond to the communication paths, as described in [38]. This way, scalable load balancing algorithms similar to those discussed in [22, 45] can be straightforwardly applied to the graph. For a more detailed discussion of the implementation of the parallel data structures we refer to [12, 15, 38].

## 2.2 Generalization of HHG towards non-nodal discretizations

The performance and scalability of the HHG prototype framework and the corresponding data structures has been studied in [14, 15, 13, 29, 30, 31]; matrix-free methods and applications have been discussed in [8, 10, 11] and [35, 53, 54]. These articles have demonstrated that HHG can reach scalability on the largest available core and node counts. However, so far the HHG principle was limited to low order nodal finite elements.

A major contribution of this article is the presentation of extended HHG data structures and to demonstrate how the HHG paradigm can be extended and augmented to support more general discretizations. A crucial point here is that the uniform refinement can be mapped to efficient linearized data structures. This becomes a key step to implement efficient kernel routines for all data that is located on the edges, faces, or within a cell of each grid element. In this article, we focus on the realization of edge-centered unknowns in the HHG architecture. Based on this software extension, we then implement quadratic, conforming finite elements. We point out that the described concepts can be transferred also to face or cell-unknowns for further generalizations and as they are needed for other finite-element discretizations.

To reveal their uniform structure, we split the edges of a refined tetrahedron into seven subgroups, corresponding to the seven different orientations of edges that are created during the refinement. We denote the groups as x-, y-, z-, xy-, xz-, yz-, and xyz-edges - named after the coordinate directions in which they are spanned. Each of these subgroups shares the properties of the nodal layout of the HHG meshes: the neighboring elements of each edge-unknown of one group have identical geometries. Therefore, employing a  $\mathbf{P}_2$  finite element discretization, we get eight different stencils per tetrahedron, including the vertex-centered stencil, see fig. 3. This uniform structure is also present on the interface-primitives. Therefore, a matrix-free implementation of classical point-smoothers such as the Gauss-Seidel method can be realized for all unknowns.

While all groups of unknowns (including vertex unknowns) can be organized in a tetrahedral layout, the number of unknowns in one tetrahedron differs per group. Since the number of vertices on each outer edge of the refined tetrahedron is equal, we define

$$N_{\text{tet}}(v) := ((v + 2)(v + 1)v)/6 \quad (7)$$

as the number of vertices in a refined tetrahedron with  $v$  vertices on the outer edge. Table 1 lists the number of unknowns for each sub-group. Note, that the number of

sub-group	inner unknowns	including boundary
vertices	$N_{\text{tet}}(2^\ell - 3)$	$N_{\text{tet}}(2^\ell + 1)$
xyz-edges	$N_{\text{tet}}(2^\ell - 1)$	$N_{\text{tet}}(2^\ell - 1)$
other edges	$N_{\text{tet}}(2^\ell - 2)$	$N_{\text{tet}}(2^\ell)$

Table 1: Number of unknowns in a tetrahedron, with and without boundary.

unknowns of a  $\mathbf{P}_2$  finite-element discretization on level  $\ell$  is equal to the numbers of unknowns of a  $\mathbf{P}_1$  finite-element discretization on level  $\ell + 1$ .

To estimate the number of floating-point operations that are required to perform matrix-vector multiplications with the different blocks of the discrete Stokes operator in eq. (5) we count the stencil entries, i.e. the number of non-zero entries in the respective row of the system matrix. We only consider the stencils in the refined macro-cells, since in the limit, most unknowns are located there.

For different discretizations, the block-matrices of the Stokes operator map from and to different function spaces. Therefore we need to consider subsets of the stencils that are depicted in fig. 3 for different operators. In table 2 we list the number of stencil entries for the 8 different stencils.

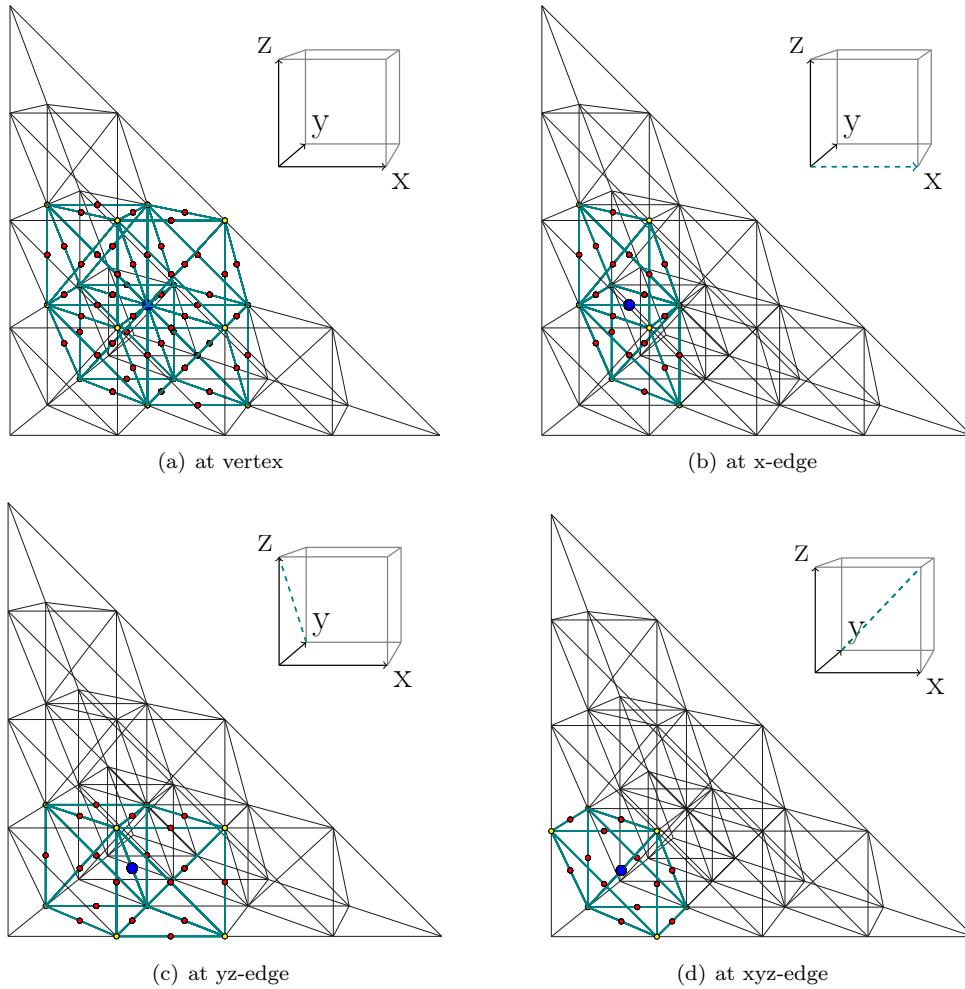


Figure 3: Neighboring elements and corresponding stencils at vertex and edge unknowns for 4 of 8 required stencils (vertex-, x-, yz-, and xyz-centered).

### 3 Matrix-free geometric multigrid

To solve the saddle point problem eq. (5) we employ a monolithic geometric multigrid method. By monolithic, we express that the method acts directly on the full system, and not on individual blocks of the system matrix. Traditionally, the Stokes system is often solved using Krylov subspace methods such as the Schur-complement conjugate gradient method or preconditioned MINRES solvers [26], which might in turn employ multigrid on the positive definite submatrix  $\mathbf{A}$  of  $\mathcal{A}$  in eq. (5). Both alternatives have been compared to a monolithic multigrid implementation on HHG in [29], where it was shown that the monolithic multigrid solver outperforms both Krylov methods in terms of time-to-solution and memory consumption. Therefore we will here focus solely on the monolithic multigrid approach, extending the results in [29, 31] to the stable mixed  $\mathbf{P}_2 - \mathbf{P}_1$  discretization.

#### 3.1 Full multigrid

We focus on the FMG scheme to achieve an asymptotically optimal complexity [19, 33, 50]. The algorithmic structure of the FMG algorithm is described in algorithm 1. The number of smoothing iterations performed by the embedded *variable* v-cycle

		to (stencil center)							
		vertex	x-e	y-e	z-e	xy-e	xz-e	yz-e	xyz-e
from	vertex	15	8	6	8	8	6	8	6
	all	65	27	19	27	27	19	27	19

Table 2: Number of stencil entries for the 8 different stencils as shown in fig. 3. The first row only includes the stencil entries that are located on vertex unknowns.

increases on the coarser grids. As described in [25], we observe that this is necessary to achieve satisfactory convergence.

**Algorithm 1** FMG algorithm to solve eq. (5) on level  $L$ . For readability, we set  $\underline{\mathbf{x}}_\ell := (\underline{\mathbf{u}}_\ell, \underline{\mathbf{p}}_\ell)^\top$ , and  $\underline{\mathbf{b}}_\ell := (\underline{\mathbf{f}}_\ell, \underline{\mathbf{g}}_\ell)^\top$ .

---

```

1: procedure FMG( $\nu_{\text{pre}}, \nu_{\text{post}}, \nu_{\text{inc}}, \kappa, \bar{A}, \bar{\xi}$ )
2:   solve  $\mathcal{A}_0 \underline{\mathbf{x}}_0 = \underline{\mathbf{b}}_0$ 
3:   for  $\ell = 1$  to  $L$  do
4:      $\underline{\mathbf{x}}_\ell = I_{\ell-1}^\ell \underline{\mathbf{x}}_{\ell-1}$  ▷ FMG interpolation
5:     repeat  $\kappa$  times
6:        $\underline{\mathbf{x}}_\ell \leftarrow \text{VAR-V-CYCLE}(\ell, \ell, \nu_{\text{pre}}, \nu_{\text{post}}, \nu_{\text{inc}}, \bar{A}, \bar{\xi}, \underline{\mathbf{x}}_\ell, \underline{\mathbf{b}}_\ell)$ 
7:   return  $\underline{\mathbf{x}}_L$ 

8: procedure VAR-V-CYCLE( $\ell_{\text{fine}}, \ell, \nu_{\text{pre}}, \nu_{\text{post}}, \nu_{\text{inc}}, \bar{A}, \bar{\xi}, \underline{\mathbf{x}}_\ell, \underline{\mathbf{b}}_\ell$ )
9:   if  $\ell = 0$  then
10:    solve  $\mathcal{A}_0 \underline{\mathbf{x}}_0 = \underline{\mathbf{b}}_0$  ▷ coarse grid solve
11:   else
12:     $\nu_{\text{pre}} + (\ell_{\text{fine}} - \ell)\nu_{\text{inc}}$  iterations of eq. (8) on  $\underline{\mathbf{x}}_\ell$  with  $(\hat{A}, \hat{\xi}) = (\bar{A}, \bar{\xi})$  ▷ relaxation
13:     $\underline{\mathbf{r}}_{\ell-1} = I_{\ell-1}^{\ell-1} (\underline{\mathbf{b}}_\ell - \mathcal{A}_\ell \underline{\mathbf{x}}_\ell)$  ▷ defect restriction
14:     $\hat{\underline{\mathbf{x}}}_{\ell-1} \leftarrow \text{VAR-V-CYCLE}(\ell_{\text{fine}}, \ell - 1, \nu_{\text{pre}}, \nu_{\text{post}}, \nu_{\text{inc}}, \bar{A}, \bar{\xi}, 0, \underline{\mathbf{r}}_{\ell-1})$ 
15:     $\underline{\mathbf{x}}_\ell \leftarrow \underline{\mathbf{x}}_\ell + I_{\ell-1}^\ell \hat{\underline{\mathbf{x}}}_{\ell-1}$  ▷ prolongation and correction
16:     $\nu_{\text{post}} + (\ell_{\text{fine}} - \ell)\nu_{\text{inc}}$  iterations of eq. (8) on  $\underline{\mathbf{x}}_\ell$  with  $(\hat{A}, \hat{\xi}) = (\bar{A}, \bar{\xi})$  ▷ relaxation
17:   return  $\underline{\mathbf{x}}_\ell$ 

```

---

## 3.2 Relaxation

Because of its saddle-point structure, the system of eq. (5) is not positive definite, and classical smoothers for scalar elliptic problems cannot be employed directly. Numerous different smoothers have been developed that can treat the saddle-point problem in a multigrid framework such as inexact Uzawa-type smoothers [28, 25], Braess-Sarazin smoothers [17] and Vanka-type block-smoothers [51]. Often, these methods use preconditioners on the individual block-matrices that require their diagonals. Chebyshev smoothers can be employed as an efficient alternative [1, 42]; they do not require the matrix diagonal and can be implemented in tensor-product approaches using matrix-vector products that can be realized efficiently on modern parallel architectures [27]. In the HHG framework, however, we represent the discrete operators by means of stencils that are either stored block-wise if the operator is (block-wise) constant, or assembled on-the-fly [10, 11]. Therefore the diagonal entries of the system matrix are available for every row of the matrix, and smoothers based on matrix-splitting can be realized.

In this work, we employ an *inexact Uzawa*-type smoother [41, 28, 25] directly to eq. (5). This algorithm has shown excellent performance as a smoother for extreme-scale multigrid methods on HHG in [9, 10, 29, 30]. It is defined as the iteration



(dropping the level index  $\ell$  in this section)

$$\begin{bmatrix} \mathbf{u}_{k+1} \\ \mathbf{p}_{k+1} \end{bmatrix} = \begin{bmatrix} \mathbf{u}_k \\ \mathbf{p}_k \end{bmatrix} + \mathcal{P}^{-1} \left( \begin{bmatrix} \mathbf{f} \\ \mathbf{g} \end{bmatrix} - \mathcal{A} \begin{bmatrix} \mathbf{u}_k \\ \mathbf{p}_k \end{bmatrix} \right), \quad \mathcal{P} = \begin{bmatrix} \hat{\mathbf{A}} & \mathbf{0} \\ \mathbf{B} & -\hat{S} \end{bmatrix}, \quad (8)$$

where  $\mathcal{A}$  is the discrete Stokes system matrix from eq. (5), and  $\hat{\mathbf{A}}$  and  $\hat{S}$  are approximations of  $\mathbf{A}$  and the Schur complement  $S = \mathbf{B}\mathbf{A}^{-1}\mathbf{B}^\top + C$ , respectively. One iteration of eq. (8) is then split into two steps:

$$\mathbf{u}_{k+(j+1)/\xi} = \mathbf{u}_{k+j/\xi} + \hat{\mathbf{A}}^{-1} \left( \mathbf{f} - \mathbf{A}\mathbf{u}_{k+j/\xi} - \mathbf{B}^\top \mathbf{p}_k \right), \quad (9)$$

$$\mathbf{p}_{k+1} = \mathbf{p}_k - \hat{S}^{-1} (\mathbf{g} - \mathbf{B}\mathbf{u}_{k+1} + C\mathbf{p}_k), \quad (10)$$

with  $\xi \in \mathbb{N}^+$ , and  $j = 0, \dots, \xi - 1$ .

In a multigrid context, we are interested in the smoothing property of the iteration, and choose  $\hat{\mathbf{A}}$  and  $\hat{S}$  as follows:  $\mathbf{A}^{-1}$  is approximated by  $\xi \geq 1$  Gauss-Seidel iterations, i. e. relaxation on  $\mathbf{A}\mathbf{u} = \mathbf{f} - \mathbf{B}^\top \mathbf{p}$ . We consider different versions for the smoother  $\hat{\mathbf{A}}^{-1}$  in eq. (9): a standard Gauss-Seidel relaxation denoted by  $\hat{\mathbf{A}} := \hat{\mathbf{A}}_f$ , and a symmetric iteration, i. e. one forward and one backward Gauss-Seidel iteration, denoted by  $\hat{\mathbf{A}} := \hat{\mathbf{A}}_s$ .

Regarding the pressure update eq. (10), we set  $\hat{S} := \omega^{-1} \text{diag}(-C)$  where  $C$  is the stabilization matrix defined in eq. (6) [25]. The relaxation parameter  $\omega^{-1}$  is set to an estimate of the maximum absolute eigenvalue of the eigenvalue problem

$$M_L^{-1} (C + \mathbf{B}\hat{\mathbf{A}}_s^{-1}\mathbf{B}^\top) \mathbf{v} = \lambda \mathbf{v} \quad (11)$$

where  $M_L$  is the lumped mass-matrix resulting from a linear finite element discretization [25]. For the analysis of the smoothing property of the inexact Uzawa iteration, we refer to [28, 25].

### 3.3 Grid transfer

The interpolation  $I_\ell^{\ell+1}$  from level  $\ell$  to  $\ell+1$  is chosen according to the order of the finite-element discretization of the prolonged function. For functions discretized with  $\mathbf{P}_2$  finite elements, we employ quadratic interpolation, linear interpolation otherwise. The velocity and pressure functions are interpolated independently. The restriction is defined as  $I_{\ell+1}^\ell := (I_\ell^{\ell+1})^\top$ .

## 4 Textbook multigrid efficiency

As introduced in section 1, our FMG method achieves TME, if it solves the system of interest, in this case eq. (5), with

$$\mathfrak{W}(\text{FMG}) / \mathfrak{W}(\mathcal{A}) < 10.$$

In this section, we quantify the computational cost of the proposed FMG iteration in algorithm 1 for both, the equal-order and Taylor-Hood finite-element discretizations, to find configurations that achieve TME.

### 4.1 Operator application

We derive a model for the computational cost of our FMG solver, starting with an approximation of the computational cost of the application of a linear operator. Therefore, we count the number of involved arithmetic operations. In the following, we compute the cost of operator applications only in the interior of a tetrahedron

on refinement level  $\ell$ . The number of unknowns in the interior of a tetrahedron is calculated using eq. (7) and table 1.

For the application of a stencil with  $n$  entries, we account  $n$  multiplications and  $n - 1$  additions. We approximate this with  $2n$  operations for each stencil application. Where necessary, the number of operations is then multiplied by three, accounting for the three velocity components.

The computational costs for the application of the block operators of eq. (5) for the  $\mathbf{P}_2 - \mathbf{P}_1$  discretization on level  $\ell$  are (cf. tables 1 and 2)

$$\mathfrak{W}(\mathbf{B}_\ell^{\mathbf{P}_2 - \mathbf{P}_1}) = \overbrace{3}^{\text{vel. components}} \cdot \underbrace{(2)}_{\text{add + mul}} \cdot \overbrace{65}^{\text{stencil size}} \cdot \underbrace{N_{\text{tet}}(2^\ell - 3)}_{\text{inner unknowns}} \quad (12)$$

$$\mathfrak{W}(\mathbf{A}_\ell^{\mathbf{P}_2 - \mathbf{P}_1}) = 3 \cdot ((2 \cdot 65) \cdot N_{\text{tet}}(2^\ell - 3) + (2 \cdot 146) \cdot N_{\text{tet}}(2^\ell - 2) + (2 \cdot 19) \cdot N_{\text{tet}}(2^\ell - 1)) \quad (13)$$

$$\mathfrak{W}(C_\ell^{\mathbf{P}_2 - \mathbf{P}_1}) = 0. \quad (14)$$

The  $\mathbf{P}_1 - \mathbf{P}_1$  finite-element discretization leads to a 15-point stencil in the interior of a refined tetrahedron [30]. It corresponds to the vertex-centered stencil in fig. 3(a) without the entries on the edges. The computational costs for the individual blocks are therefore

$$\mathfrak{W}(\mathbf{A}_\ell^{\mathbf{P}_1 - \mathbf{P}_1}) = \mathfrak{W}(\mathbf{B}_\ell^{\mathbf{P}_1 - \mathbf{P}_1}) = 3 \cdot (2 \cdot 15) \cdot N_{\text{tet}}(2^\ell - 3) \quad (15)$$

$$\mathfrak{W}(C_\ell^{\mathbf{P}_1 - \mathbf{P}_1}) = (2 \cdot 15) \cdot N_{\text{tet}}(2^\ell - 3). \quad (16)$$

While  $\mathfrak{W}(\mathbf{B}_\ell) \neq \mathfrak{W}(\mathbf{B}_\ell^\top)$  because of boundary effects, they asymptotically incur the same cost, i. e. we approximate  $\mathfrak{W}(\mathbf{B}_\ell) \approx \mathfrak{W}(\mathbf{B}_\ell^\top)$ .

The cost of an application of a block matrix is approximated with the sum of the work for the application of the individual blocks. For  $\mathcal{A}_\ell$  of eq. (5) we set

$$\mathfrak{W}(\mathcal{A}_\ell) \approx \mathfrak{W}(\mathbf{A}_\ell) + \mathfrak{W}(\mathbf{B}_\ell^\top) + \mathfrak{W}(\mathbf{B}_\ell) + \mathfrak{W}(C_\ell).$$

To set these numbers into perspective, we compare the cost of the application of the Stokes operator discretized with  $\mathbf{P}_2 - \mathbf{P}_1$  finite elements on level  $\ell$  with the cost of the operator application for the PSPG stabilized  $\mathbf{P}_1 - \mathbf{P}_1$  discretization on level  $\ell + 1$ . As stated in section 2, the number of unknowns for a  $\mathbf{P}_2$  finite-element discretization on level  $\ell$  equals the number of unknowns for a  $\mathbf{P}_1$  discretization on level  $\ell + 1$ . However, in both formulations for the Stokes problem, the pressure is discretized linearly. The asymptotic ratio of unknowns ( $\mathbf{P}_2 - \mathbf{P}_1 / \mathbf{P}_1 - \mathbf{P}_1$ ) for a level ratio  $\ell / (\ell + 1)$  is (cf. table 1)

$$\lim_{\ell \rightarrow \infty} \frac{3 \cdot (N_{\text{tet}}(2^\ell - 3) + 6 \cdot N_{\text{tet}}(2^\ell - 2) + N_{\text{tet}}(2^\ell - 1)) + N_{\text{tet}}(2^\ell - 3)}{4 \cdot N_{\text{tet}}(2^{\ell+1} - 3)} = \frac{25}{32}.$$

The asymptotic, work ratios of the individual operator blocks of eq. (5) and the Stokes operators are

$$\lim_{\ell \rightarrow \infty} \frac{\mathfrak{W}(\mathbf{A}_\ell^{\mathbf{P}_2 - \mathbf{P}_1})}{\mathfrak{W}(\mathbf{A}_{\ell+1}^{\mathbf{P}_1 - \mathbf{P}_1})} = \frac{23}{12}, \quad \lim_{\ell \rightarrow \infty} \frac{\mathfrak{W}(\mathbf{B}_\ell^{\mathbf{P}_2 - \mathbf{P}_1})}{\mathfrak{W}(\mathbf{B}_{\ell+1}^{\mathbf{P}_1 - \mathbf{P}_1})} = \frac{13}{24}, \quad \lim_{\ell \rightarrow \infty} \frac{\mathfrak{W}(\mathcal{A}_\ell^{\mathbf{P}_2 - \mathbf{P}_1})}{\mathfrak{W}(\mathcal{A}_{\ell+1}^{\mathbf{P}_1 - \mathbf{P}_1})} = \frac{9}{10}. \quad (17)$$

Concluding, the work for the application of the two operators  $\mathcal{A}_\ell^{\mathbf{P}_2 - \mathbf{P}_1}$  and  $\mathcal{A}_{\ell+1}^{\mathbf{P}_1 - \mathbf{P}_1}$  is comparable.

## 4.2 Multigrid

It follows the estimation of the computational work of the FMG algorithm as listed in algorithm 1.

**Relaxation** First, we only regard the work of the relaxation eq. (8), which we denote as  $\mathfrak{W}(\mathcal{P}_\ell^{-1})$ . The velocity update eq. (9) is decomposed into the application of the discrete gradient  $\mathbf{B}_\ell^\top$  and the relaxation with  $\hat{\mathbf{A}}_\ell$ . The pressure update eq. (10) is split into the application of the discrete divergence  $\mathbf{B}_\ell$  and multiplication with  $\hat{S}_\ell^{-1}$ . We neglect the application of  $\hat{S}_\ell^{-1}$  in our calculations, since it corresponds to a diagonal scaling.

The computational work for a single (forward or backward) Gauss-Seidel iteration is approximated with the computational work of the application of the corresponding operator. The inverse of the diagonal entries of  $\mathbf{A}_\ell$  can be precomputed and stored since we are considering constant coefficients, therefore no additional division has to be counted. We set (dropping the level index  $\ell$  for readability)

$$\mathfrak{W}(\mathbf{A}) \approx \mathfrak{W}(\hat{\mathbf{A}}_f^{-1}) = \frac{1}{2}\mathfrak{W}(\hat{\mathbf{A}}_s^{-1}).$$

The cost for one iteration of the Uzawa relaxation eq. (8) is approximated by

$$\mathfrak{W}(\mathcal{P}_\ell^{-1}) \approx \mathfrak{W}(\hat{\mathbf{A}}_\ell^{-1}) + \mathfrak{W}(\mathbf{B}_\ell^\top) + \mathfrak{W}(\mathbf{B}_\ell) + \mathfrak{W}(C_\ell).$$

**Variable v-cycle** We now turn our attention to the cost analysis of the variable v-cycle as defined in algorithm 1. The goal is to estimate the cost of one iteration by the work that is performed on the finest grid. The computational work of a single variable v-cycle iteration with finest level  $L$  is denoted by  $\mathfrak{W}(V^L)$ . The work that is performed only on level  $\ell$ , is denoted by  $\mathfrak{W}(V_\ell^L)$ , i. e.  $\mathfrak{W}(V^L) = \sum_{\ell=0}^L \mathfrak{W}(V_\ell^L)$ .

We neglect the computational work that is required to compute the exact solution on the coarsest level  $\ell = 0$  since it is, in theory, given a sufficiently coarse grid, not a performance bottleneck. Also, the grid transfer is neglected in our model, since in practice, the execution time is strongly dominated by the remaining components. For the residual calculation, we account the cost of one operator evaluation  $\mathfrak{W}(\mathcal{A}_\ell)$ . Overall the cost of the variable v-cycle on a single level  $\ell \in \{0, \dots, L\}$  is

$$\mathfrak{W}(V_\ell^L) = (\nu_{\text{pre}} + \nu_{\text{post}} + 2(L - \ell)\nu_{\text{inc}}) \mathfrak{W}(\mathcal{P}_\ell^{-1}) + \mathfrak{W}(\mathcal{A}_\ell).$$

Recursively, we approximate (asymptotically, the number of grid points increases by a factor of 8 per level)

$$\mathfrak{W}(V_{L-q}^L) \approx \frac{1}{8^q} (\mathfrak{W}(V_L^L) + 2q\nu_{\text{inc}}\mathfrak{W}(\mathcal{P}_L^{-1})), \quad q \in \{0, \dots, L\}$$

and provide an upper bound  $\mathfrak{W}^*(V^L)$  to the cost of a variable v-cycle on level  $L$  by

$$\begin{aligned} \mathfrak{W}(V^L) &= \sum_{\ell=0}^L \mathfrak{W}(V_\ell^L) \lesssim \sum_{q=0}^{\infty} \frac{1}{8^q} (\mathfrak{W}(V_L^L) + 2q\nu_{\text{inc}}\mathfrak{W}(\mathcal{P}_L^{-1})) \\ &= \frac{8}{7}\mathfrak{W}(V_L^L) + \frac{16}{49}\nu_{\text{inc}}\mathfrak{W}(\mathcal{P}_L^{-1}) =: \mathfrak{W}^*(V^L). \end{aligned} \quad (18)$$

**Full multigrid** Using eq. (18), and  $\mathfrak{W}(V_\ell^L) \approx 8\mathfrak{W}(V_{\ell-1}^L)$ , an upper bound to the cost of the FMG iteration with finest level  $L$  is given by

$$\begin{aligned} \mathfrak{W}(\text{FMG}^L) &= \sum_{\ell=0}^L \kappa \mathfrak{W}(V_\ell^L) \lesssim \kappa \sum_{q=0}^{\infty} \frac{1}{8^q} \left( \frac{8}{7}\mathfrak{W}(V_L^L) + \frac{16}{49}\nu_{\text{inc}}\mathfrak{W}(\mathcal{P}_L^{-1}) \right) \\ &= \frac{8\kappa}{7}\mathfrak{W}^*(V^L). \end{aligned}$$

**Normalization to work units** Our goal is to express the cost of the FMG iteration in WU as defined in eq. (1). The cost in WU of an operator or iterative scheme  $D$  normalized by the cost of an operator  $H$  is in the following denoted by

$$\mathfrak{W}_H(D) := \mathfrak{W}(D) / \mathfrak{W}(H).$$

Of particular interest, is normalization with regards to the work of  $\mathcal{A}^{\mathbf{P}_2 - \mathbf{P}_1}$  and  $\mathcal{A}^{\mathbf{P}_1 - \mathbf{P}_1}$ . Using eqs. (12) to (14), the normalized cost of the individual blocks and smoothers are

$$\mathfrak{W}_{\mathcal{A}^{\mathbf{P}_2 - \mathbf{P}_1}}(\mathbf{A}^{\mathbf{P}_2 - \mathbf{P}_1}) \xrightarrow{\ell \rightarrow \infty} \frac{46}{72}, \quad \mathfrak{W}_{\mathcal{A}^{\mathbf{P}_2 - \mathbf{P}_1}}(\mathbf{B}^{\mathbf{P}_2 - \mathbf{P}_1}) \xrightarrow{\ell \rightarrow \infty} \frac{13}{72}.$$

for the  $\mathbf{P}_2 - \mathbf{P}_1$  discretization, and

$$\mathfrak{W}_{\mathcal{A}^{\mathbf{P}_1 - \mathbf{P}_1}}(\mathbf{A}^{\mathbf{P}_1 - \mathbf{P}_1}) \xrightarrow{\ell \rightarrow \infty} \frac{3}{10}, \quad \mathfrak{W}_{\mathcal{A}^{\mathbf{P}_1 - \mathbf{P}_1}}(C^{\mathbf{P}_1 - \mathbf{P}_1}) \xrightarrow{\ell \rightarrow \infty} \frac{1}{10}$$

with  $\mathfrak{W}_{\mathcal{A}^{\mathbf{P}_1 - \mathbf{P}_1}}(\mathbf{A}^{\mathbf{P}_1 - \mathbf{P}_1}) = \mathfrak{W}_{\mathcal{A}^{\mathbf{P}_1 - \mathbf{P}_1}}(\mathbf{B}^{\mathbf{P}_1 - \mathbf{P}_1})$  in the PSPG stabilized case (cf. eqs. (15) and (16)).

For the  $\mathbf{P}_2 - \mathbf{P}_1$  finite element discretization, the cost of an Uzawa relaxation  $\mathfrak{W}_{\mathbf{P}_2 - \mathbf{P}_1}(\mathcal{P}^{-1})$  using a forward Gauss-Seidel relaxation ( $\hat{\mathbf{A}} = \hat{\mathbf{A}}_f$ ,  $\xi = 1$ ) and a symmetric version ( $\hat{\mathbf{A}} = \hat{\mathbf{A}}_s$ ,  $\xi = 1$ ) therefore account for 1 WU and  $\frac{118}{72}$  WU respectively.

Exemplarily, the cost of the FMG iteration for the  $\mathbf{P}_2 - \mathbf{P}_1$  discretization of the Stokes problem parameterized as  $\text{FMG}(1, 1, 2, 1, \hat{\mathbf{A}}_s, 1)$  (cf. algorithm 1) can be calculated as

$$\mathfrak{W}_{\mathbf{P}_2 - \mathbf{P}_1}(\text{FMG}(1, 1, 2, 1, \hat{\mathbf{A}}_s, 1)) = \frac{8}{7} \left( \frac{8}{7} ((1 + 1 + 0) \frac{118}{72} + 1) + \frac{16}{49} \cdot 2 \cdot \frac{118}{72} \right) \approx 6.8$$

which would, if the system were solved sufficiently, indicate TME according to eq. (2). In the following section, we experiment with different configurations to assess the quality of our solver with respect to TME.

## 5 Performance analysis of the multigrid solver

In this section, we address the numerical efficiency and computational performance of the inexact-Uzawa multigrid solver. Two benchmarks are considered to assess the efficiency of our solver with regard to TME. Finally we present a roofline analysis of the employed relaxation kernels and demonstrate the extreme scalability of the implementation.

All benchmarks in this section are performed and reproducible with the open source framework HYTEG<sup>1</sup> [38], which implements all data structures and solvers described in this article. For the coarse grid solvers, we utilize the Portable, Extensible Toolkit for Scientific Computation (PETSc)<sup>2</sup> [4].

### 5.1 Numerical efficiency

The convergence rate of an iterative solver alone does not permit any statement about its numerical efficiency, as long as the involved computational work is not considered. In this section, both metrics, i. e. convergence and computational work are combined to assess, and optimize numerical efficiency of the proposed multigrid solver, and, at best, reach TME.

<sup>1</sup><https://i10git.cs.fau.de/hyteg/hyteg>, Git-SHA: a8e393e8

<sup>2</sup><https://www.mcs.anl.gov/petsc/>

Let  $x$  define a continuous, exact solution for the underlying PDE,  $\mathbf{x}_{\ell,j}^*$  the evaluation of  $x$  at grid node  $j$  on level  $\ell$ , and  $I_\ell^{\ell+1}$  as in section 3.3. The discrete  $L^2$ -error  $\|\mathbf{e}(\tilde{\mathbf{x}}_\ell)\|_2$  of a computed solution  $\tilde{\mathbf{x}}_\ell$  is in the following defined as

$$\|\mathbf{e}(\tilde{\mathbf{x}}_\ell)\|_2 := \|\mathbf{x}_{\ell+1}^* - I_\ell^{\ell+1}\tilde{\mathbf{x}}_\ell\|_2, \quad \|\mathbf{x}_\ell\|_2 = \sqrt{\mathbf{x}_\ell^\top \mathbf{M}_\ell \mathbf{x}_\ell}, \quad (19)$$

where  $\mathbf{M}_\ell$  is the corresponding finite-element mass-matrix on level  $\ell$ . The interpolation to a finer grid is performed to reflect the continuity of the finite-element solution in the error. Let  $\mathbf{x}_\ell$  a solution of the considered linear system  $\mathcal{A}\mathbf{x}_\ell = \mathbf{b}_\ell$  with  $(\mathbf{r}_u, \mathbf{r}_p)^\top = \mathbf{b}_\ell - \mathcal{A}\mathbf{x}_\ell$  and  $\|\mathbf{r}_u\|_2 < \epsilon \wedge \|\mathbf{r}_p\|_2 < \epsilon$ . We define  $\gamma(\tilde{\mathbf{x}}_\ell)$  as the ratio of the error of a computed solution  $\tilde{\mathbf{x}}_\ell$  to the discretization error,

$$\gamma(\tilde{\mathbf{x}}_\ell) := \|\mathbf{e}(\tilde{\mathbf{x}}_\ell)\|_2 / \|\mathbf{e}(\mathbf{x}_\ell)\|_2.$$

We set for our experiments  $\epsilon = 10^{-12}$ . A well-parameterized FMG solver should reduce the error of the solution, so that  $\gamma(\tilde{\mathbf{x}}_\ell)$  is close to 1 [50, 29].

Our aim is to achieve TME, i. e. find parameterizations  $s$  with  $\mathfrak{W}(\text{FMG}(s)) < 10$ , for which the FMG iteration *solves the underlying PDE* up to discretization accuracy. Solving the discrete system exactly is usually much more expensive, however, not relevant, since the discretization error dominates the approximation. We loosely consider the PDE eq. (3) solved, if the computed solution  $(\mathbf{u}_\ell, \mathbf{p}_\ell)$  of eq. (5) satisfies  $\gamma(\mathbf{u}_\ell), \gamma(\mathbf{p}_\ell) \leq 2$ . Clearly, lower bounds can be achieved, and may be desired, too. In general, we expect  $\mathfrak{W}(\text{FMG}(s))$  to inversely depend on the chosen bounds to  $\gamma(\mathbf{u}_\ell)$  and  $\gamma(\mathbf{p}_\ell)$ . Finding a *numerically efficient* FMG solver, can be viewed as a multi-objective optimization problem, in this case with objectives  $\mathfrak{W}(\text{FMG}(s))$ ,  $\gamma(\mathbf{u}_\ell)$ , and  $\gamma(\mathbf{p}_\ell)$ .

To find efficient parameterizations, we define a parameter search space  $S = \{(\bar{v}_{\text{pre}}, \bar{v}_{\text{post}}, \bar{v}_{\text{inc}}, \bar{\kappa}, \bar{\mathbf{A}}, \bar{\xi}) : 0 \leq \bar{v}_{\text{pre}}, \bar{v}_{\text{post}}, \bar{v}_{\text{inc}} \leq 3, 1 \leq \bar{\kappa} \leq 2, (\bar{\mathbf{A}}, \bar{\xi}) \in \{(\hat{\mathbf{A}}_f, 1), (\hat{\mathbf{A}}_f, 2), (\hat{\mathbf{A}}_f, 3), (\hat{\mathbf{A}}_f, 4), (\hat{\mathbf{A}}_s, 1), (\hat{\mathbf{A}}_s, 2)\}\}$ , containing 768 tuples.

We employ the Multifrontal Massively Parallel sparse direct Solver (MUMPS) [23], interfaced through PETSc [4] as a direct solver for the unstructured coarse grid ( $\ell = 0$ ).

### 5.1.1 Cube with analytical solution

As in [31], we consider an analytical solution for eq. (3) on the cube  $\Omega = (0, 1)^3$ :

$$\begin{aligned} \mathbf{u} &= (-4 \cos(4x_3), 8 \cos(8x_1), -2 \cos(2x_2))^\top, \\ p &= \sin(4x_1) \sin(8x_2) \sin(2x_3) + \text{const} \end{aligned}$$

with the right-hand side  $\mathbf{f}$  that satisfies eq. (3), and  $\partial\Omega_D = \partial\Omega$ . The cube is partitioned into 24 macro-tetrahedra, that are uniformly refined  $L$  times, resulting in about  $4.3 \times 10^6$  unknowns for the  $\mathbf{P}_1 - \mathbf{P}_1$  discretization ( $L = 6$ ) and  $3.4 \times 10^6$  unknowns for the  $\mathbf{P}_2 - \mathbf{P}_1$  discretization ( $L = 5$ ). The relaxation parameter  $\omega^{-1}$  is estimated by 100 power iterations on eq. (11), resulting in  $\omega^{-1} = 0.448872$  for the  $\mathbf{P}_2 - \mathbf{P}_1$  and  $\omega^{-1} = 0.570751$  for the  $\mathbf{P}_1 - \mathbf{P}_1$  discretization.

In table 3, we list some configurations found by optimizing for minimal computational work of the resulting FMG iteration, while prescribing upper bounds  $\hat{\gamma}_u$  and  $\hat{\gamma}_p$  for  $\gamma(\mathbf{u}_L)$  and  $\gamma(\mathbf{p}_L)$ . Also, we fixed  $\kappa = 1$ , since frequent visits of the coarse grids generally decrease the performance in parallel settings, and allowing  $\kappa = 2$  does not substantially reduce the minimal work obtained.

The results for both discretizations are satisfactory, as TME is achieved, or almost achieved for all chosen upper bounds in table 3. Notably, for the  $\mathbf{P}_2 - \mathbf{P}_1$  case, at least 3 inner Gauss-Seidel iterations in eq. (9) seem to be favorable, and especially increasing the number of post-smoothing steps appears to improve the efficiency of the

$\mathbf{P}_1 - \mathbf{P}_1, L = 6, \min_{s \in \hat{S}}(\mathfrak{W}(\text{FMG}(s))), \hat{S} := \{s \in S : \kappa = 1 \wedge \gamma(\underline{\mathbf{u}}_L) \leq \hat{\gamma}_u \wedge \gamma(\underline{\mathbf{p}}_L) \leq \hat{\gamma}_p\}$				
$(\hat{\gamma}_u, \hat{\gamma}_p)$	(1.1, 2)	(1.1, 5)	(2, 10)	
$s$	$(2, 3, 2, 1, \hat{\mathbf{A}}_s, 1)$	$(3, 1, 3, 1, \hat{\mathbf{A}}_s, 1)$	$(1, 0, 2, 1, \hat{\mathbf{A}}_s, 1)$	
$\mathfrak{W}(\text{FMG}(s))$	10.77	9.55	3.97	
$\gamma(\underline{\mathbf{u}}_L)$	1.10	1.10	1.62	
$\gamma(\underline{\mathbf{p}}_L)$	1.51	2.91	8.52	

$\mathbf{P}_2 - \mathbf{P}_1, L = 5, \min_{s \in \hat{S}}(\mathfrak{W}(\text{FMG}(s))), \hat{S} := \{s \in S : \kappa = 1 \wedge \gamma(\underline{\mathbf{u}}_L) \leq \hat{\gamma}_u \wedge \gamma(\underline{\mathbf{p}}_L) \leq \hat{\gamma}_p\}$				
$(\hat{\gamma}_u, \hat{\gamma}_p)$	(1.1, 2)	(1.1, 5)	(2, 10)	
$s$	$(1, 3, 2, 1, \hat{\mathbf{A}}_f, 3)$	$(1, 2, 1, 1, \hat{\mathbf{A}}_f, 3)$	$(0, 2, 1, 1, \hat{\mathbf{A}}_f, 3)$	
$\mathfrak{W}(\text{FMG}(s))$	14.91	11.08	8.11	
$\gamma(\underline{\mathbf{u}}_L)$	1.01	1.02	1.47	
$\gamma(\underline{\mathbf{p}}_L)$	1.99	4.55	9.81	

Table 3: Results for some parameterizations from the search space  $S$ , optimized towards minimal work with fixed upper bounds for  $\gamma(\underline{\mathbf{u}}_L)$  and  $\gamma(\underline{\mathbf{p}}_L)$ , and  $\kappa = 1$ .

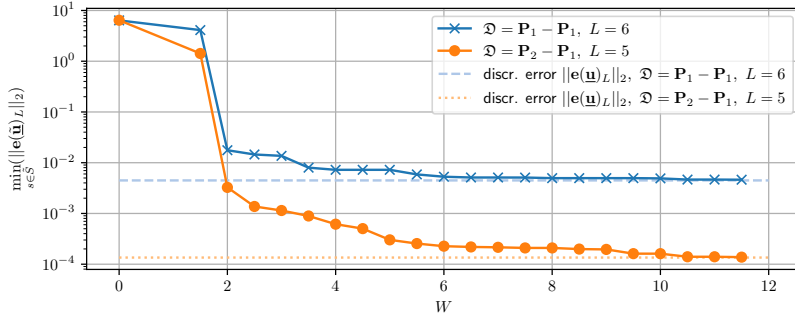


Figure 4: Minimal achievable velocity error after an FMG iteration with parameterization  $s \in S$  that requires a maximum work of  $W$ , plotted for  $W \in \{0\} \cup \{1.5, 2, \dots, 12\}$ . Precisely,  $\min_{s \in \hat{S}}(\|\mathbf{e}(\tilde{\mathbf{u}}_L)\|_2)$  with  $\hat{S} := \{s \in S : \mathfrak{W}(\text{FMG}(s)) \leq W\}$ , and discretization  $\mathfrak{D}$  on level  $L$ .

iteration. For both discretizations, a looser bound to the pressure error significantly reduces the required work. If only a very accurate velocity solution is of interest, very efficient parameterizations may be chosen. We note that no configuration could reduce the pressure error so that  $\gamma(\underline{\mathbf{p}}_L) \leq 1.4$ . Similar results for the  $\mathbf{P}_1 - \mathbf{P}_1$  discretization are presented and discussed in [31, 30].

Table 3 lacks a direct comparison of the efficiency among the two discretizations. Again, we are interested in *solving the PDE*, and not in the exact solution of the discrete problem. To this end, the ratios  $\gamma(\underline{\mathbf{u}}_\ell)$  and  $\gamma(\underline{\mathbf{p}}_\ell)$  fail to express a discretization-invariant, quantitative measure for accuracy of the computed solution. The ratio eq. (17) suggests, that a similar amount of work is required to apply either  $\mathcal{A}_\ell^{\mathbf{P}_2 - \mathbf{P}_1}$  or  $\mathcal{A}_{\ell+1}^{\mathbf{P}_1 - \mathbf{P}_1}$ . We compare therefore the error  $\|\mathbf{e}(\tilde{\mathbf{u}}_L)\|_2$  as defined in eq. (19) after applying the FMG iteration to solve eq. (5) with  $\mathcal{A}_L = \mathcal{A}_L^{\mathbf{P}_2 - \mathbf{P}_1}$ ,  $L = 5$ , and  $\mathcal{A}_L = \mathcal{A}_L^{\mathbf{P}_1 - \mathbf{P}_1}$  with  $L = 6$ . In particular, we plot in fig. 4 the minimal velocity error  $\|\mathbf{e}(\tilde{\mathbf{u}}_L)\|_2$  that can be achieved with an FMG configuration that requires a certain maximum amount of work  $W$ . For the considered example, the  $\mathbf{P}_1 - \mathbf{P}_1$  discretization accuracy on level  $L = 6$  is reached even for really efficient configurations of the FMG solver when employing the  $\mathbf{P}_2 - \mathbf{P}_1$  discretization on level  $L = 5$ . For example, a 10-fold reduction of the low-order discretization error is achieved with  $\mathfrak{W}_{\mathbf{P}_2 - \mathbf{P}_1}(\text{FMG}) \approx 5$ .

### 5.1.2 Flow through a junction

As a second benchmark problem, we consider a y-shaped junction, that is slightly bent in z-direction, with a single, sinusoidal inflow and two natural outflow (Neumann)

$s$	$\mathbf{P}_2 - \mathbf{P}_1, L = 4$		
	$(1, 3, 2, 1, \hat{\mathbf{A}}_f, 3)$	$(1, 2, 1, 1, \hat{\mathbf{A}}_f, 3)$	$(0, 2, 1, 1, \hat{\mathbf{A}}_f, 3)$
$\mathfrak{W}(\text{FMG}(s))$	14.91	11.08	8.11
$\delta(\underline{\mathbf{u}}_L)$	0.10%	0.12%	0.19%
$\delta(\underline{\mathbf{p}}_L)$	5.37%	6.39%	9.40%

Table 4: Relative errors for velocity and pressure as defined in eq. (20) for computed solutions for the junction domain. The FMG configurations are chosen as in table 3.

boundaries, cf. fig. 5. For this benchmark the  $\mathbf{P}_2 - \mathbf{P}_1$  discretization is employed.

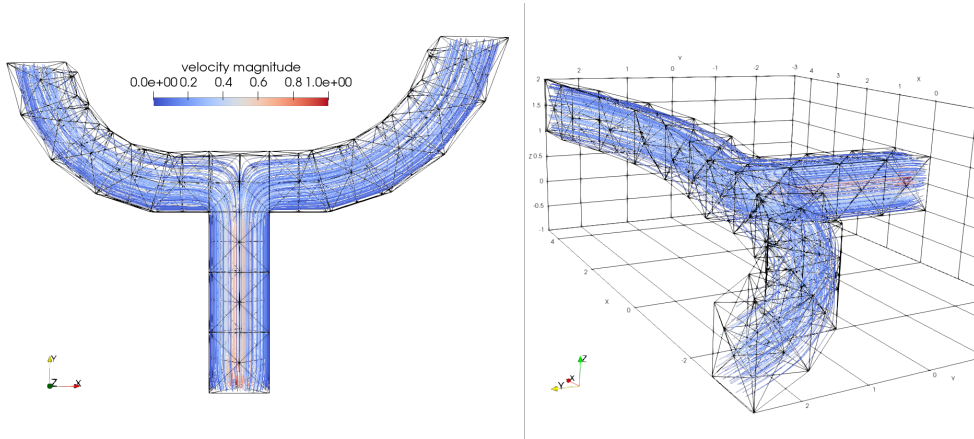


Figure 5: Domain and computed solution of the flow through a y-shaped junction.

The domain consists of 336 coarse grid tetrahedra, that are each refined  $L = 4$  times, resulting in a system with  $5.9 \times 10^6$  unknowns (including boundary). Since no analytical solution is available, we assess the FMG solver by measuring the relative error  $\delta$  of the computed (velocity and pressure) solution  $\tilde{\mathbf{x}}_\ell$ , to a given solution  $\mathbf{x}_\ell$  that reduces the velocity and pressure residual so that  $\|\underline{\mathbf{r}}_u\|_2 < \epsilon \wedge \|\underline{\mathbf{r}}_p\|_2 < \epsilon$ ,  $\epsilon = 10^{-12}$  (cf. section 5.1), defined as

$$\delta(\mathbf{x}_\ell) := \|\tilde{\mathbf{x}}_\ell - \mathbf{x}_\ell\|_2 / \|\mathbf{x}_\ell\|_2. \quad (20)$$

The estimation of  $\omega^{-1}$  with eq. (11) does not yield good results, so we set  $\omega^{-1} = 0.2$  empirically.

In table 4, we list the relative errors for velocity and pressure for the parameterizations found in table 3. Similarly to the results of the first benchmark problem, the relative velocity error is reduced successfully below 0.2% after only a single FMG iteration. The pressure error remains above 5% for all settings, which can be considered insufficient, if the pressure solution is of interest in the respective application. Overall, the solver shows a similar qualitative behavior for a different domain.

## 5.2 Computational performance

This last section briefly covers the computational performance on the node-level and the parallel scalability. In particular, we are concerned with the implementation of the kernels and HHG data structures for the  $\mathbf{P}_2 - \mathbf{P}_1$  discretization. The performance and scalability for the linear, equal-order discretization is e.g. analyzed in [30, 29]. We note, that a more concise, in-depth performance analysis on top of the theoretical results is important, but out of the scope of this article and subject to future work.

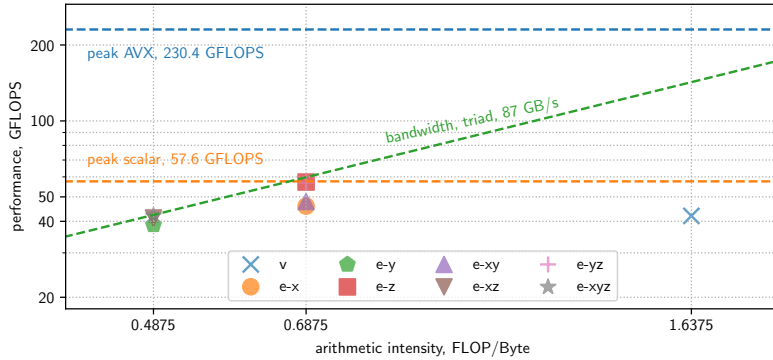


Figure 6: Roofline plot containing all 8 kernels employed in the Gauss-Seidel relaxation.

### 5.2.1 Node-level performance

Efficient node-level execution is key to fast and scalable numerical code. Parallel code based on slow compute kernels performs well in scaling experiments, and in fact, a poor parallel scalability can be hidden by introducing redundant work that slows down the kernel performance [2, 34]. Therefore, in our approach we first strive to achieve the best possible node-level performance before we target scalability.

The roofline model [34, 55] provides a simplified, and optimistic tool to predict the maximal possible performance of a compute kernel implementation. The corresponding upper bounds are either prescribed by the computational peak performance or the memory bandwidth of the machine. To analyze the node-level performance of our multigrid implementation, we conduct a roofline analysis for the compute kernels of the Gauss-Seidel implementation.

The implementation of the Gauss-Seidel iteration is split into 8 kernels, each of which updates one group of unknowns as introduced in section 2.2. We measure the performance of each kernel individually, applied to 8 macro-cells in parallel, that are refined 8 times respectively. The measurements are performed on an Intel<sup>®</sup> Xeon<sup>®</sup> Gold 5122 CPU, with 2 sockets, and 8 cores in total. Communication is not included in the measurements. To obtain the performance of the kernels, and bandwidth of the machine, we use the *likwid*<sup>3</sup> [49] tools (version 4.3.4).

In fig. 6, the results of the roofline analysis are plotted, together with the measured bandwidth, and the theoretical peak, and scalar peak performance of the machine. With a fixed clock rate of 3.60 GHz, 8 cores, AVX-256, and 2 fused multiply-adds (FMA) per cycle we get a theoretical peak of 230.4 GFLOPS. All 7 kernels that update the edge unknowns are memory-bound, the implementation reaches the bandwidth limit in almost all cases. *likwid* reports at least 95% – 98% of the performed FLOP originate from AVX instructions, for the edge-centered kernels. The kernel applying the vertex-centered stencil is, due to its high arithmetic intensity, not memory bound. However, it cannot be vectorized because of the lexicographic update pattern and is therefore expected to be bound by the scalar peak performance; *likwid* reports 75% of scalar peak performance.

We emphasize, that the roofline model tends to estimate optimistic upper performance bounds. While it gives a first impression of the performance, refined approaches like the Execution-Cache-Memory (ECM) model provide more realistic estimates [46].

<sup>3</sup><https://github.com/RRZE-HPC/likwid>



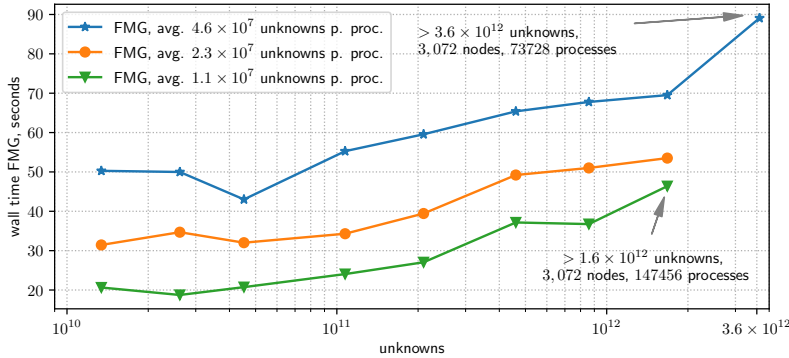


Figure 7: Weak and strong scaling of the FMG solver with  $(\nu_{pre}, \nu_{post}, \nu_{inc}, \kappa, \hat{\mathbf{A}}, \xi) = (0, 2, 1, 1, \hat{\mathbf{A}}_f, 3)$ .

### 5.2.2 Parallel scalability

Finally, we demonstrate strong and weak scaling results of the FMG implementation. The scaling experiments are conducted on the thin nodes of SuperMUC-NG, which is ranked 13<sup>th</sup> in the Top500 as of June 2020<sup>4</sup>. Each node is equipped with two Intel<sup>®</sup> Skylake Xeon<sup>®</sup> Platinum 8174 CPU, i.e. a total of 48 cores per node, and 96GB main memory. In total, the machine operates 6,336 (thin) nodes; we have access to a maximum of 3,072 nodes. For the scalability experiment, we run the benchmark as described in section 5.1.1, with finer coarse grids, to balance the number of macro-primitives among the parallel processes, and 7-times refined tetrahedra.

Figure 7 shows the wall time for the FMG solver for the  $\mathbf{P}_2-\mathbf{P}_1$  discretization, and  $(\nu_{pre}, \nu_{post}, \nu_{inc}, \kappa, \hat{\mathbf{A}}, \xi) = (0, 2, 1, 1, \hat{\mathbf{A}}_f, 3)$ . A weak scaling of three configurations is presented:  $1.1 \times 10^7$ ,  $2.3 \times 10^7$ , and  $4.6 \times 10^7$  unknowns per process on average. For the latter scenario, the number of processes per node is reduced from 48 to 24.

We demonstrate scalability to all available 147,456 processes, and, in the largest scenario, solve a Stokes system with more than  $3.6 \times 10^{12}$  unknowns in about 90 seconds. The solution vector alone requires more than 28TB of main memory. The monolithic multigrid solver with inexact Uzawa relaxation is especially suited for large scale computations, as it can be implemented with only one additional temporary vector, on top of the solution and right-hand side.

We emphasize, that such extreme scalability can only be achieved with matrix-free solvers, and careful choice and implementation of the corresponding algorithms and data structures [29].

## 6 Conclusion

We demonstrate in this article, that TME can be achieved for different discretizations of the Stokes problem, while maintaining high computational performance and low memory overhead. The relevant data structures to realize scalable matrix-free implementations, also for higher-order finite-element discretizations, are introduced. Two benchmark problems show, that a satisfactory error reduction of the velocity component can be achieved with computational work that is of the order of 10 discrete operator applications. The computational efficiency and parallel scalability of the implementation is presented by a roofline analysis, and weak and strong scaling experiments, demonstrate scalability to up to 147,456 parallel processes and systems with more than  $3.6 \times 10^{12}$  unknowns. This article may serve as a basis for further anal-

<sup>4</sup><https://www.top500.org/>

ysis of the efficiency of Stokes solvers, in particular for the case of varying coefficients and for coupled, possibly non-linear applications.

## Acknowledgements

The authors gratefully acknowledge the Gauss Centre for Supercomputing e.V. (<https://www.gauss-centre.eu>) for funding this project by providing computing time on the GCS Supercomputer SuperMUC-NG at Leibniz Supercomputing Centre (<https://www.lrz.de>).

## References

- [1] Mark Adams, Marian Brezina, Jonathan Hu, and Ray Tuminaro. Parallel multigrid smoothing: polynomial versus gauss–seidel. *Journal of Computational Physics*, 188(2):593–610, 2003.
- [2] David H Bailey. Misleading performance claims in parallel computations. In *Proceedings of the 46th Annual Design Automation Conference*, pages 528–533. ACM, 2009.
- [3] Allison H Baker, Axel Klawonn, Tzanio Kolev, Martin Lanser, Oliver Rheinbach, and Ulrike Meier Yang. Scalability of classical algebraic multigrid for elasticity to half a million parallel tasks. In *Software for Exascale Computing – SPPEXA 2013–2015*, pages 113–140. Springer, 2016.
- [4] Satish Balay, William D. Gropp, Lois Curfman McInnes, and Barry F. Smith. Efficient Management of Parallelism in Object Oriented Numerical Software Libraries. In E. Arge, A. M. Bruaset, and H. P. Langtangen, editors, *Modern Software Tools in Scientific Computing*, pages 163–202. Birkhäuser Press, 1997.
- [5] Peter Bastian, Eike Hermann Müller, Steffen Müthing, and Marian Pitkowski. Matrix-free multigrid block-preconditioners for higher order discontinuous Galerkin discretisations. *Journal of Computational Physics*, 394:417–439, 2019.
- [6] Martin Bauer, Sebastian Eibl, Christian Godenschwager, Nils Kohl, Michael Kuron, Christoph Rettinger, Florian Schornbaum, Christoph Schwarzmeier, Dominik Thönnies, Harald Köstler, et al. waLBerla: A block-structured high-performance framework for multiphysics simulations. *Computers & Mathematics with Applications*, 2020.
- [7] Simon Bauer, Hans-Peter Bunge, Daniel Drzisga, Siavash Ghelichkhan, Markus Huber, Nils Kohl, Marcus Mohr, Ulrich Rüde, Dominik Thönnies, and Barbara Wohlmuth. TerraNeo — mantle convection beyond a trillion degrees of freedom. *Software for Exascale Computing SPPEXA*, page 569, 2020.
- [8] Simon Bauer, Daniel Drzisga, Marcus Mohr, U Rüde, Christian Waluga, and Barbara Wohlmuth. A stencil scaling approach for accelerating matrix-free finite element implementations. *SIAM Journal on Scientific Computing*, 40(6):C748–C778, 2018.
- [9] Simon Bauer, Markus Huber, S Ghelichkhan, Marcus Mohr, Ulrich Rüde, and B Wohlmuth. Large-scale simulation of mantle convection based on a new matrix-free approach. *Journal of Computational Science*, 31:60–76, 2019.

- [10] Simon Bauer, Markus Huber, Marcus Mohr, Ulrich Rüde, and Barbara Wohlmuth. A new matrix-free approach for large-scale geodynamic simulations and its performance. In *International Conference on Computational Science*, pages 17–30. Springer, 2018.
- [11] Simon Bauer, Marcus Mohr, Ulrich Rüde, Jens Weismüller, Markus Wittmann, and Barbara Wohlmuth. A two-scale approach for efficient on-the-fly operator assembly in massively parallel high performance multigrid codes. *Applied Numerical Mathematics*, 122:14–38, 2017.
- [12] B. Bergen and F. Hülsemann. Hierarchical hybrid grids: A framework for efficient multigrid on high performance architectures. *Technical Report, Lehrstuhl für Systemsimulation, Universität Erlangen*, 5, 2003.
- [13] Benjamin Bergen. *Hierarchical Hybrid Grids: Data structures and core algorithms for efficient finite element simulations on supercomputers*. Advances in simulation. SCS Publishing House, 2006.
- [14] Benjamin Bergen, Tobias Gradl, Frank Hülsemann, and Ulrich Rüde. A massively parallel multigrid method for finite elements. *Computing in science & engineering*, 8(6):56–62, 2006.
- [15] Benjamin Bergen and Frank Hülsemann. Hierarchical hybrid grids: data structures and core algorithms for multigrid. *Numerical linear algebra with applications*, 11(2-3):279–291, 2004.
- [16] Jürgen Bey. Tetrahedral grid refinement. *Computing*, 55(4):355–378, 1995.
- [17] Dietrich Braess and Regina Sarazin. An efficient smoother for the Stokes problem. *Applied Numerical Mathematics*, 23(1):3–19, 1997.
- [18] A. Brandt. *Barriers to achieving textbook multigrid efficiency (TME) in CFD*. Institute for Computer Applications in Science and Engineering, NASA Langley Research Center, 1998.
- [19] Achi Brandt and Oren E. Livne. *Multigrid techniques: 1984 guide with applications to fluid dynamics*, volume 67. SIAM, 2011.
- [20] Franco Brezzi and Jim Douglas. Stabilized mixed methods for the Stokes problem. *Numerische Mathematik*, 53(1-2):225–235, 1988.
- [21] Jed Brown. Efficient nonlinear solvers for nodal high-order finite elements in 3D. *Journal of Scientific Computing*, 45(1-3):48–63, 2010.
- [22] Carsten Burstedde, Lucas C Wilcox, and Omar Ghattas. p4est: Scalable algorithms for parallel adaptive mesh refinement on forests of octrees. *SIAM Journal on Scientific Computing*, 33(3):1103–1133, 2011.
- [23] Alfredo Buttari, Markus Huber, Philippe Leleux, Théo Mary, Ulrich Rüde, and Barbara Wohlmuth. Block Low Rank Single Precision Coarse Grid Solvers for Extreme Scale Multigrid Methods. working paper or preprint, April 2020.
- [24] Tony F Chan, Tarek P Mathew, et al. Domain decomposition algorithms. *Acta numerica*, 3(1):61–143, 1994.
- [25] Daniel Drzisga, Lorenz John, Ulrich Rüde, Barbara Wohlmuth, and Walter Zulehner. On the analysis of block smoothers for saddle point problems. *SIAM Journal on Matrix Analysis and Applications*, 39(2):932–960, 2018.

- [26] Howard C Elman, David J Silvester, and Andrew J Wathen. *Finite elements and fast iterative solvers: with applications in incompressible fluid dynamics*. Oxford University Press, USA, 2014.
- [27] Niklas Fehn, Wolfgang A Wall, and Martin Kronbichler. Efficiency of high-performance discontinuous galerkin spectral element methods for under-resolved turbulent incompressible flows. *International Journal for Numerical Methods in Fluids*, 88(1):32–54, 2018.
- [28] Francisco J Gaspar, Yvan Notay, Cornelis W Oosterlee, and Carmen Rodrigo. A simple and efficient segregated smoother for the discrete Stokes equations. *SIAM journal on scientific computing*, 36(3):A1187–A1206, 2014.
- [29] Björn Gmeiner, Markus Huber, Lorenz John, Ulrich Rüde, and Barbara Wohlmuth. A quantitative performance study for Stokes solvers at the extreme scale. *Journal of Computational Science*, 17:509–521, 2016.
- [30] Björn Gmeiner, Ulrich Rüde, Holger Stengel, Christian Waluga, and Barbara Wohlmuth. Performance and scalability of hierarchical hybrid multigrid solvers for Stokes systems. *SIAM Journal on Scientific Computing*, 37(2):C143–C168, 2015.
- [31] Björn Gmeiner, Ulrich Rüde, Holger Stengel, Christian Waluga, and Barbara Wohlmuth. Towards textbook efficiency for parallel multigrid. *Numerical Mathematics: Theory, Methods and Applications*, 8(1):22–46, 2015.
- [32] Christian Godenschwager, Florian Schornbaum, Martin Bauer, Harald Köstler, and Ulrich Rüde. A framework for hybrid parallel flow simulations with a trillion cells in complex geometries. In *Proceedings of the International Conference on High Performance Computing, Networking, Storage and Analysis*, pages 1–12, 2013.
- [33] Wolfgang Hackbusch. *Iterative solution of large sparse systems of equations*, volume 95. Springer, 1994.
- [34] Georg Hager and Gerhard Wellein. *Introduction to high performance computing for scientists and engineers*. CRC Press, 2010.
- [35] Markus Huber, Ulrich Rüde, Christian Waluga, and Barbara Wohlmuth. Surface couplings for subdomain-wise isoviscous gradient based Stokes finite element discretizations. *Journal of Scientific Computing*, 74(2):895–919, 2018.
- [36] Thomas JR Hughes, Leopoldo P Franca, and Marc Balestra. A new finite element formulation for computational fluid dynamics: V. circumventing the Babuška-Brezzi condition: A stable Petrov-Galerkin formulation of the Stokes problem accommodating equal-order interpolations. *Computer Methods in Applied Mechanics and Engineering*, 59(1):85–99, 1986.
- [37] Axel Klawonn, Martin Lanser, and Oliver Rheinbach. Toward extremely scalable nonlinear domain decomposition methods for elliptic partial differential equations. *SIAM Journal on Scientific Computing*, 37(6):C667–C696, 2015.
- [38] Nils Kohl, Dominik Thönnnes, Daniel Drzisga, Dominik Bartuschat, and Ulrich Rüde. The HyTeG finite-element software framework for scalable multigrid solvers. *International Journal of Parallel, Emergent and Distributed Systems*, 34(5):477–496, 2019.
- [39] Martin Kronbichler and Katharina Kormann. A generic interface for parallel cell-based finite element operator application. *Computers & Fluids*, 63:135–147, 2012.

- [40] Sebastian Kuckuk and Harald Köstler. Automatic generation of massively parallel codes from exaslang. *Computation*, 4(3):27, 2016.
- [41] JF Maitre, F Musy, and P Nigon. A fast solver for the Stokes equations using multigrid with a Uzawa smoother. In *Advances in Multi-Grid Methods*, pages 77–83. Springer, 1985.
- [42] Dave A May, Jed Brown, and Laetitia Le Pourhiet. A scalable, matrix-free multigrid preconditioner for finite element discretizations of heterogeneous Stokes flow. *Computer methods in applied mechanics and engineering*, 290:496–523, 2015.
- [43] Ulrich Rüde, Karen Willcox, Lois Curfman McInnes, and Hans De Sterck. Research and education in computational science and engineering. *Siam Review*, 60(3):707–754, 2018.
- [44] Johann Rudi, A Cristiano I Malossi, Tobin Isaac, Georg Stadler, Michael Gurnis, Peter WJ Staar, Yves Ineichen, Costas Bekas, Alessandro Curioni, and Omar Ghattas. An extreme-scale implicit solver for complex PDEs: highly heterogeneous flow in earth’s mantle. In *Proceedings of the international conference for high performance computing, networking, storage and analysis*, pages 1–12, 2015.
- [45] Florian Schornbaum and Ulrich Rüde. Extreme-scale block-structured adaptive mesh refinement. *SIAM Journal on Scientific Computing*, 40(3):C358–C387, 2018.
- [46] Holger Stengel, Jan Treibig, Georg Hager, and Gerhard Wellein. Quantifying performance bottlenecks of stencil computations using the execution-cache-memory model. In *Proceedings of the 29th ACM on International Conference on Supercomputing*, pages 207–216. ACM, 2015.
- [47] Cedric Taylor and Paul Hood. A numerical solution of the Navier-Stokes equations using the finite element technique. *Computers & Fluids*, 1(1):73–100, 1973.
- [48] James L Thomas, Boris Diskin, and Achi Brandt. Textbook multigrid efficiency for fluid simulations. *Annual review of fluid mechanics*, 35(1):317–340, 2003.
- [49] J. Treibig, G. Hager, and G. Wellein. Likwid: A lightweight performance-oriented tool suite for x86 multicore environments. In *Proceedings of PSTI2010, the First International Workshop on Parallel Software Tools and Tool Infrastructures*, San Diego CA, 2010.
- [50] Ulrich Trottenberg, Cornelius W Oosterlee, and Anton Schuller. *Multigrid*. Elsevier, 2000.
- [51] S Pratap Vanka. Block-implicit multigrid solution of Navier-Stokes equations in primitive variables. *Journal of Computational Physics*, 65(1):138–158, 1986.
- [52] Rüdiger Verfürth. A multilevel algorithm for mixed problems. *SIAM journal on numerical analysis*, 21(2):264–271, 1984.
- [53] Christian Waluga, Barbara Wohlmuth, and Ulrich Rüde. Mass-corrections for the conservative coupling of flow and transport on collocated meshes. *Journal of Computational Physics*, 305:319–332, 2016.
- [54] Jens Weismüller, Björn Gmeiner, Siavash Ghelichkhan, Markus Huber, Lorenz John, Barbara Wohlmuth, Ulrich Rüde, and Hans-Peter Bunge. Fast asthenosphere motion in high-resolution global mantle flow models. *Geophysical Research Letters*, 42(18):7429–7435, 2015.

- [55] Samuel Williams, Andrew Waterman, and David Patterson. Roofline: an insightful visual performance model for multicore architectures. *Communications of the ACM*, 52(4):65–76, 2009.
- [56] Barbara I Wohlmuth. Iterative solvers based on domain decomposition. In *Discretization Methods and Iterative Solvers Based on Domain Decomposition*, pages 85–176. Springer, 2001.